Available online at www.sciencedirect.com
ScienceDirect
Earth and Planetary Science Letters 268 (2008) 515–525
EPSL
www.elsevier.com/locate/epsl

Deformation and texture development in $CaIrO_3$ post-perovskite phase up to 6 GPa and 1300 K

Lowell Miyagi [a,*], Norimasa Nishiyama [c], Yanbin Wang [c], Atsushi Kubo [b], Don V. West [d], Robert J. Cava [d], Thomas S. Duffy [b], Hans-Rudolf Wenk [a]

[a] Department of Earth and Planetary Science, University of California, Berkeley, CA 94720, USA
[b] Department of Geosciences, Princeton University, Princeton, NJ 08544, USA
[c] Center for Advanced Radiation Sources, University of Chicago, Chicago, IL 60637, USA
[d] Department of Chemistry, Princeton University, Princeton, NJ 08544, USA

Received 1 August 2007; received in revised form 19 January 2008; accepted 3 February 2008
Available online 16 February 2008
Editor: G.D. Price

Abstract

At near ambient conditions, $CaIrO_3$ is isostructural with the high-pressure polymorph $MgSiO_3$ "post-perovskite" (pPv). $MgSiO_3$ pPv is thought to be a major phase in the earth's lowermost mantle. $CaIrO_3$ can thus serve as an analog for studying deformation of the pPv phase under conditions achievable with a multi-anvil deformation apparatus. Here we study the rheologic behavior of $CaIrO_3$ pPv at a variety of pressure and temperature conditions from 2 GPa to 6 GPa and 300 K to 1300 K and various strain rates. Sintered, polycrystalline $CaIrO_3$ pPv, cylindrical in shape, was deformed in the D-DIA multi-anvil press in several shortening cycles up to 20% axial strain at each temperature and pressure. Shortening cycles were followed by lengthening back to 0% strain. Quantitative texture information was obtained using *in-situ* synchrotron X-ray diffraction and the Rietveld method to analyze images. In all cases we find that (010) lattice planes align perpendicular to the compression direction upon shortening, and that there is little change in texture with temperature or pressure. This texture pattern is consistent with slip on (010)[100]. The texture observed here is different from that produced in room temperature diamond anvil cell (DAC) experiments on $MgGeO_3$ and $MgSiO_3$ pPv which both display textures of (100) and {110} lattice planes at high angles to the compression direction. This implies that $CaIrO_3$ pPv may not be a good analog for the plastic behavior of $MgSiO_3$ pPv.

Keywords: post-perovskite; $CaIrO_3$; texture; multi-anvil press; deformation mechanism; slip; VPSC

1. Introduction

Since the discovery of the phase transition in $MgSiO_3$ from a perovskite (Pv) to a post-perovskite (pPv) structure at 127 GPa and 2500 K (Murakami et al., 2004; Oganov and Ono, 2004), there has been considerable interest in the mechanical properties of the pPv structure. $MgSiO_3$ pPv may be a major constituent of the D'' layer which lies above the core–mantle boundary. The D'' is a region characterized by a seismic discontinuity that also exhibits significant lateral heterogeneity and seismic anisotropy (Wysession et al., 1998; Lay et al., 1998; Sidorin et al., 1999; Panning and Romanowicz, 2004). First-principles calculations using density functional theory and available experiments suggest that pPv single crystals exhibit strong elastic anisotropy (Murakami et al., 2004; Oganov and Ono, 2004; Stackhouse et al., 2005; Wentzcovitch et al., 2006; Shieh et al., 2006; Guignot et al., 2007).

One mechanism that can generate seismic anisotropy in the earth is the development of lattice preferred orientation (LPO) or texture during plastic deformation of aggregates composed of anisotropic minerals. A texture pattern generated in this way depends on the deformation geometry as well as deformation mechanisms. Radial diffraction patterns obtained *in-situ* during

* Corresponding author.
E-mail address: miyagi@eps.berkeley.edu (L. Miyagi).

0012-821X/$ - see front matter © 2008 Elsevier B.V. All rights reserved.
doi:10.1016/j.epsl.2008.02.005

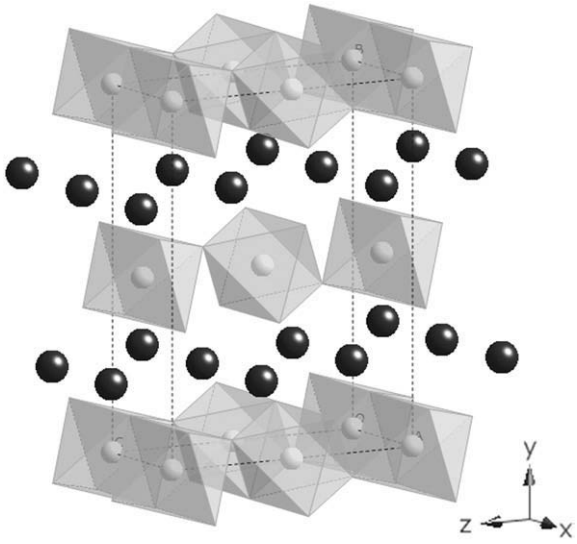

Fig. 1. The crystal structure (Cmcm) of $CaIrO_3$ pPv. Note the layering normal to the *y*-axis. Black spheres are calcium and the grey octahedra are IrO_6.

deformation experiments with diamond anvil cells (DAC) have been used successfully to observe texture changes and infer active slip systems (e.g. Wenk et al., 2006). Since $MgSiO_3$ pPv is unquenchable to ambient conditions, deformation studies are both difficult and limited and investigation of analog materials is of interest. $CaIrO_3$ is stable in the pPv structure (Fig. 1) at ambient conditions (Rodi and Bable, 1965), making it a potentially useful analog.

Based on the layered structure it has been suggested that the pPv structure should slip along the layers (Fig. 1), on the (010) plane (Murakami et al., 2004; Oganov and Ono, 2004; Iitaka et al., 2004). First-principles calculations of dislocation cores based on the Peierls–Nabarro model found (010)[001] to be the easy slip system in $MgSiO_3$ pPv (Carrez et al., 2007). However, Oganov et al. (2005) predicted slip on {110} using first-principles metadynamics and energetics of stacking faults. Room temperature DAC deformation experiments found textures consistent with {110} slip in $MgGeO_3$ pPv (Merkel et al., 2006) and $MgSiO_3$ pPv (Merkel et al., 2007). A transmission electron microscopy (TEM) study of dislocation microstructures generated during synthesis of $CaIrO_3$ pPv identified Burgers vectors $\mathbf{b}=[100]$ and suggested that (010) might be the likely slip plane (Miyajima et al., 2006). Yamazaki et al. (2006) performed field emission scanning electron microscopy (FE-SEM) and electron backscatter diffraction (EBSD) analysis on $CaIrO_3$ pPv samples recovered from high-temperature shear experiments and inferred the (010)[100] slip system based on fabric observations. This was confirmed by EBSD and TEM work on samples recovered from high-temperature coaxial shortening and simple shear experiments in the D-DIA to a higher pressure of 3 GPa (Walte et al., 2007). Recent DAC experiments on $CaIrO_3$ pPv at room temperature and up to 6 GPa obtained textures that also suggest (010) slip (Niwa et al., 2007). Differences in the slip systems observed for high-temperature deformation of $CaIrO_3$ pPv and room temperature DAC experiments on other pPv phases could be due to a different dominant slip-system at high-temperature in the pPv structure (Yamazaki et al., 2006). It is also conceivable that DAC experiments could be recording transformation textures (Santillián et al., 2006; Walte et al., 2007) or could even be due to development under lower differential stress or annealing (Santillián et al., 2006).

Samples can be subjected to a range of pressures and temperatures using the D-DIA (Wang et al., 2003). The D-DIA is cubic multi-anvil device in which two of the six anvils can be controlled independently (Fig. 2). This allows the user to increase pressure quasi-hydrostatically and also impose axial differential stresses. Compared with the DAC, this device also has the advantage that it can be used to deform relatively large samples while controlling or monitoring pressure, stress, temperature, strain rate, and total strain. Here we report on texture development of $CaIrO_3$ pPv observed *in-situ* during controlled deformation in the D-DIA at a range of pressures and temperatures.

2. Experimental procedure

Polycrystalline $CaIrO_3$ pPv was synthesized from a 1:1 molar ratio of CaO and IrO_2 by first heating in a vacuum-sealed silica tube to 1250 K at ambient pressure for 68 h. The result was a sample composed of a non-stoichiometric mixture of oxides, $CaIrO_3$ Pv, and pPv. This sample was then compressed to 7 GPa at 1370 K for 4 h in a large-volume press at beamline 13ID-D of the GSECARS sector at the Advanced Photon Source (APS). This yielded a pre-sintered and stoichiometric polycrystalline aggregate of $CaIrO_3$ pPv as confirmed by powder X-ray diffraction. Fig. 3a shows scanning electron microscopy (SEM) images of the undeformed $CaIrO_3$ pPv starting material. Prior to deformation there is a random fabric with no apparent foliation. Individual grains have a slightly platy habit but are overall relatively equiaxed. Large grains are on the order of 10–20 μm with some smaller grains of only a few μm in diameter interspersed among the larger grains.

Deformation was carried out at the 13-BM-D beamline of the GSECARS sector at the APS, using the D-DIA and a 250 ton press (Fig. 2). The X-ray beam of wavelength 0.2254Å was collimated to 200 μm × 200 μm with two pairs of tungsten

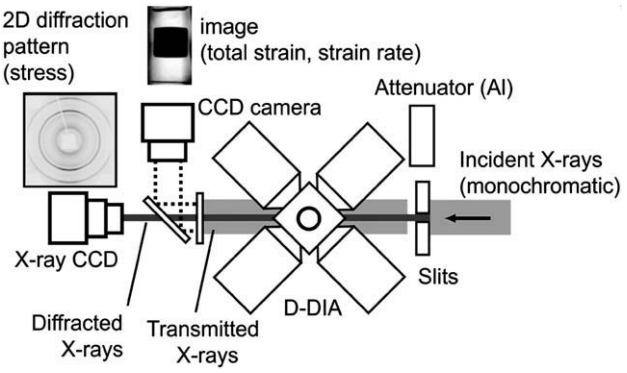

Fig. 2. Schematic of the X-ray diffraction set-up for the D-DIA multi-anvil press. The X-rays pass through the anvil gap and diffraction images are recorded on the X-ray CCD. Diffraction images contain information on texture and lattice strains. By opening the slits, wide beam radiography images can be recorded on the CCD camera and are used to measure strain. From Wang et al. (2003).

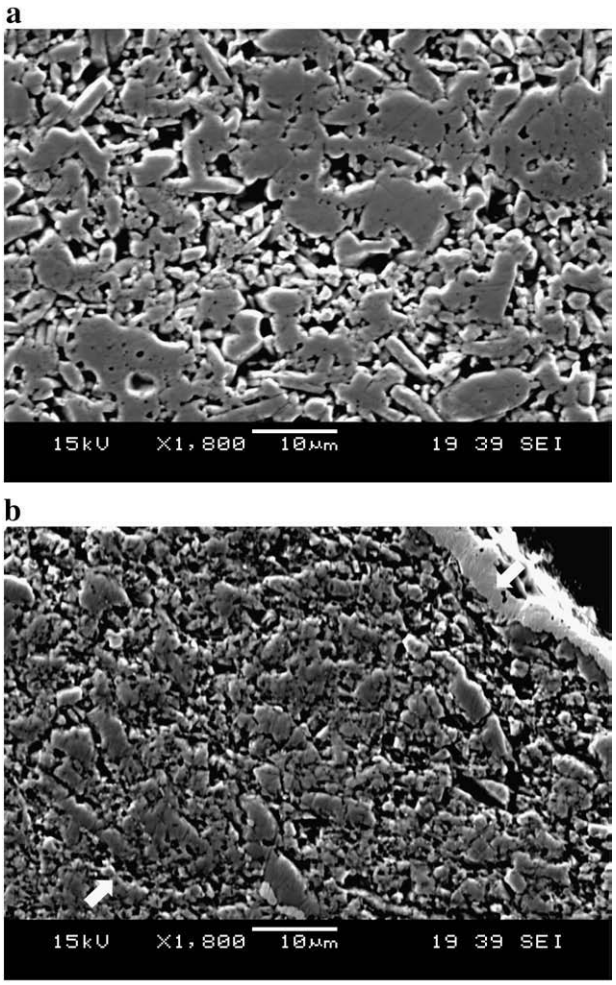

Fig. 3. SEM images of $CaIrO_3$ pPv. a) Image of undeformed sample. Grains are relatively equiaxed and the sample has a random fabric. b) Sample at the end of the experiment. Grains have been reduced in size and developed platy morphology. The sample has developed significant foliation perpendicular to the direction of compression (indicated by white arrows).

carbide (WC) slits. The beam was directed through the anvil gap and the sample assembly. Diffraction patterns were recorded using a Bruker SMART-1500, charge-coupled device (CCD) detector with 1024×1024 pixels. Spatial dimensions of the pixels were determined to be 0.09×0.09 mm. Non-orthogonality of the X-ray CCD relative to the incident beam was corrected using a CeO_2 diffraction standard. A radiographic imaging assembly was also installed, which consisted of a YAG phosphor (15 mm diameter and 0.2 mm thick), a mirror oriented at a 45° angle relative to the phosphor, and a MicroMAX CCD camera with an objective lens. The imaging CCD had 1030×1024 pixels, with a spatial resolution of about 0.002 mm. Using this system, sample length could be measured by driving out the WC collimating slits to provide a wide beam (2×3 mm). Throughout the course of the experiment an automatic routine was executed to alternate between collecting diffraction and radiographic images by driving the slits and corresponding optical components in or out of the beam path. This way changes in texture and lattice strains could be measured and correlated to macroscopic strain.

The cylindrical $CaIrO_3$ pPv sample (1 mm in diameter and 1.2 mm in length) was polished on both ends to ensure that the sample ends were parallel and perpendicular to the cylindrical axis. The sample was then loaded into a hexagonal boron nitride sleeve. Gold foils were placed at each end of the sample to serve as strain markers. Two densified alumina pistons were placed on either side of the sample, and on top of each a crushable alumina piston was placed to provide a cushion to ensure smooth compression. This assembly was loaded into a graphite sleeve, which served as a resistive heater, and then placed inside a cubic pressure medium composed of mullite with a boron-epoxy filled path to allow passage of the X-ray beam. The detector-sample distance was calibrated based on the lattice dimensions of $CaIrO_3$ at ambient conditions inside the D-DIA.

Four WC and two X-ray transparent sintered diamond anvils with truncated edge length of 4 mm were used to compress the sample. Two WC anvils were placed on the upstream side with the two sintered diamond anvils positioned downstream of the sample to allow full 360° observation of Debye rings. The sample was first compressed quasi-hydrostatically to a load of 25 tons (~2–3 GPa). At this pressure the sample was shortened $\geq 10\%$ natural strain, corresponding to $\varepsilon = 100 * \ln(l_0/l)$, where l_0 is the initial sample length after quasi-hydrostatic compression. Each cycle of shortening was followed by lengthening to return to near 0% natural strain. For the 25 ton load (~2–3 GPa), we deformed the sample at 300 K, 600 K, 800 K, and 1000 K at various strain rates by varying differential ram speeds. Following deformation at 25 tons, the load was again increased quasi-hydrostatically to 45 tons (~4–5 GPa) and the sample shortened at 300 K, 800 K, 1000 K, and 1300 K at a variety of strain rates. Ram speeds varied from 0.001 mm/s to 0.03 mm/s approximately corresponding to strain rates of $8.3 * 10^{-4}$ s^{-1} and $2.5 * 10^{-2}$ s^{-1}. Pressure was calibrated using a thermal equation of state for $CarIrO_3$ based on the high-temperature Birch–Murnaghan equation (Martin et al., 2007).

Fig. 3b shows an SEM image of the sample at the end of deformation. The platy morphology of grains has been greatly enhanced and significant reduction in grain size is observed. A strong foliation perpendicular to the shortening direction is also observed, indicating that grains have become preferentially oriented. This platy morphology in $CaIrO_3$ pPv has also been observed with the TEM (Miyajima et al., 2006) and in grain growth experiments (Yoshino and Yamazaki, 2007).

3. Data analysis

A total of 586 diffraction images were collected, of which 41 were selected for detailed analysis. The analyzed images were taken during the initial quasi-hydrostatic pressure increase, and then at minimum and maximum strain for each cycle of shortening and lengthening. Synchrotron diffraction images were analyzed using the Rietveld method as implemented in the software package MAUD (Lutterotti et al., 1999). This technique has been previously applied to analyze texture development in ringwoodite samples, deformed in the D-DIA (Wenk et al., 2005).

The diffraction images were first processed using the program Fit2d (Hammersley, 1997) and converted from polar

to Cartesian coordinates. In the "unrolled" diffraction images, variations in lattice spacings with respect to the compression direction are due to elastic strains imposed by the deformation device. These manifest themselves as sinusoidal variations in peak positions with azimuth (Fig. 4). Preferred orientation resulting from crystal rotations during plastic deformation appears as systematic intensity variations along Debye rings. If lattice planes in a sample are predominantly oriented in a particular direction then more intense diffraction will be observed in that direction. By deconvoluting this information the full orientation distribution (OD) can be determined from a single synchrotron diffraction image (Ischia et al., 2005). To analyze diffraction images using MAUD, the images are integrated over 5° azimuthal arcs into 72 spectra. For this analysis the 2θ range 2.3°–7.4° was used. Images can be refined for instrumental and structural parameters, microstructure, lattice strains and preferred orientation. Here we do not refine the structure, except for the lattice parameters, and follow a procedure similar to that outlined in Miyagi et al. (2006) with the following additional consideration. When using the D-DIA, the X-ray beam passes through the anvil gaps and experiences

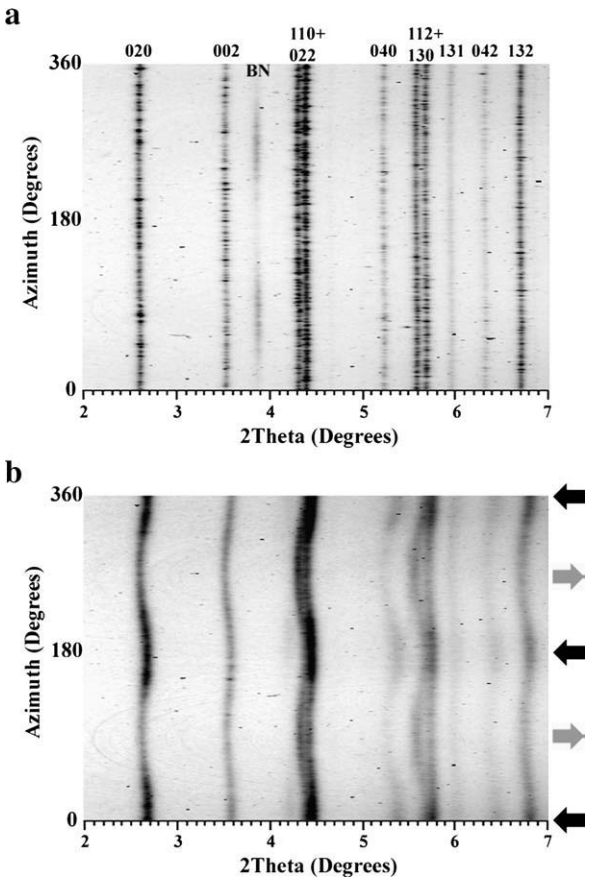

Fig. 4. a) Unrolled diffraction image of $CaIrO_3$ at the start of the experiment prior to quasi-hydrostatic compression. Sample is texture free and exhibits no apparent lattice strains. Major peaks are labeled as is one peak from the BN sleeve. b) Unrolled diffraction image after axial shortening at 25 tons and 300 K. Sinusoidal variations in peak positions due to lattice strains have developed, as have systematic intensity variations due to texture. Compression and extension directions are indicated by black and grey arrows respectively. After shortening the pattern is less spotty due to grains-size reduction.

absorption from the sample assembly. This results in direction-dependent absorption in the data that must be corrected to extract the true texture. The correction was performed by applying an individual intensity parameter to each spectrum, as well as three individual backgrounds. The intensity parameter accounts for intensity variations with azimuth that are due to absorption while the individual backgrounds correct for 2θ dependent absorption. These are in addition to global background and intensity corrections applied to the whole pattern.

For the elastic strain refinement the moment pole stress model was used with a bulk path geometric mean micro-mechanical model (Matthies et al., 2001). The moment pole stress model is similar to that of Singh (1993) and Singh et al. (1998) but takes into account the effects of preferred orientations, as well as allowing deformation geometries more complicated than pure axial compression. According to the geometry of axial compression, the stress tensor σ_{ij} can be separated into hydrostatic σ_p and differential stress D_{ij} components such that

$$\sigma_{ij} = \begin{bmatrix} \sigma_p & 0 & 0 \\ 0 & \sigma_p & 0 \\ 0 & 0 & \sigma_p \end{bmatrix} + \begin{bmatrix} -t/3 & 0 & 0 \\ 0 & -t/3 & 0 \\ 0 & 0 & 2t/3 \end{bmatrix} = \sigma_p + D_{ij}$$

where t is the axial stress component and provides a lower bounds for the yield strength of the material (Singh, 1993; Singh et al., 1998). Consequently for this refinement the differential stresses were fixed such that $\sigma_{11}=\sigma_{22}$ and $\sigma_{33}=-2\sigma_{11}$, where σ_{33} is the largest principal stress and is negative for compression, according to the conventions in MAUD. Elastic constants from Fujibuchi et al. (2006) were used for stress model calculations. Since only the pressure dependence of the C_{ij}s has been calculated, the elastic constants were not corrected for temperature in the calculation of stresses.

For texture refinement the tomographic E-WIMV algorithm was used. The E-WIMV model is similar to the WIMV model (Matthies and Vinel, 1982) but allows for incomplete and arbitrary pole figure coverage. In the case of axial compression, cylindrical symmetry about the compression axis can be assumed and textures can be compactly represented with an inverse pole figure (IPF). An IPF shows the relationship between crystallographic directions of crystallites within the sample to the compression direction. Pole densities are expressed in multiples of random distribution (m.r.d.), where 1 m.r.d. corresponds to a random distribution and in the case of a single crystal the m.r.d. would be equal to infinity. For orthorhombic materials such as $CaIrO_3$ pPv, only one quadrant of the IPF is needed to fully represent the OD.

4. Results

Refinement results for lattice parameters, axial stress component (t), and the texture index (F_2) as well corresponding deformation conditions are given in Table 1. The texture index is the squared integral over the OD and gives a measure of texture sharpness (Bunge, 1982). An F_2 of 1 indicates a random distribution and anything greater than 1 indicates a textured sample.

Table 1
Table summarizing results from Rietveld refinement

Image #	Time (h)	Load (ton)	P (GPa)	T (K)	a (Å)	b (Å)	c (Å)	Natural strain (%)	t (GPa)	F_2
19[a]	0:00:00	0	0.00	300	3.1415(0)	9.8752(0)	7.2971(0)	–	0	1.046
26	4:34:32	25	1.95	300	3.1303(2)	9.8257(6)	7.2826(4)	0.0	0.41(1)	1.066
40	6:13:31	25	4.10	300	3.1285(3)	9.7298(10)	7.2768(6)	11.0	−1.95(2)	1.132
50	7:23:19	25	1.62	300	3.1301(3)	9.8386(8)	7.2861(6)	0.6	1.00(2)	1.118
59	8:31:53	25	4.63	300	3.1272(3)	9.7127(9)	7.2729(5)	12.7	−2.42(1)	1.150
64	9:19:23	25	1.19	300	3.1323(2)	9.8523(6)	7.2878(4)	1.9	1.43(1)	1.067
66	10:33:19	25	2.22	600	3.1336(2)	9.8660(6)	7.2974(4)	−2.8	1.01(1)	1.078
75	12:01:17	25	4.08	600	3.1289(2)	9.8039(6)	7.2817(4)	5.2	−1.39(1)	1.098
84	13:04:20	25	4.83	600	3.1326(2)	9.7498(8)	7.2851(8)	15.7	−2.43(1)	1.174
85	14:06:55	25	4.46	600	3.1341(3)	9.7583(8)	7.2890(6)	17.9	−1.99(2)	1.186
97	15:31:01	25	1.75	600	3.1339(2)	9.8801(7)	7.3051(5)	−1.6	1.51(1)	1.124
98	15:48:30	25	2.11	800	3.1390(2)	9.8878(6)	7.3161(4)	−1.6	0.65(1)	1.114
140	20:47:00	25	4.04	800	3.1338(2)	9.8207(6)	7.3006(5)	20.8	−0.72(1)	1.160
146	21:29:01	25	1.51	800	3.1457(3)	9.8903(11)	7.3233(7)	3.4	0.29(2)	1.126
148	21:55:11	25	1.99	1000	3.1423(2)	9.9152(5)	7.3370(4)	−1.6	0.27(1)	1.116
184	26:08:11	25	3.15	1000	3.1403(2)	9.8710(6)	7.3261(4)	9.8	−0.49(1)	1.133
195	27:23:30	25	2.19	1000	3.1449(2)	9.9019(6)	7.3323(4)	2.0	0.26(1)	1.099
211	29:15:52	25	3.36	1000	3.1421(2)	9.8577(6)	7.3237(4)	13.5	−0.63(1)	1.137
219	30:10:06	25	0.80	1000	3.1525(2)	9.9310(6)	7.3525(4)	0.8	0.42(1)	1.089
229	31:17:36	25	3.20	1000	3.1424(2)	9.8620(6)	7.3261(4)	11.8	−0.70(1)	1.121
236	32:12:00	25	0.77	1000	3.1530(3)	9.9304(10)	7.3531(7)	0.2	0.20(1)	1.091
241	32:47:01	25	3.55	1000	3.1411(2)	9.8512(7)	7.3227(4)	10.1	−1.51(1)	1.125
247	33:30:21	25	1.91	1000	3.1461(2)	9.9094(7)	7.3358(5)	4.2	0.98(1)	1.097
249	35:15:07	45	1.87	300	3.1266(2)	9.8391(6)	7.2841(4)	1.7	1.66(1)	1.121
279	38:45:20	45	3.33	300	3.1303(3)	9.7517(11)	7.2846(8)	13.9	−3.07(2)	1.158
290	41:04:20	45	1.99	300	3.1274(2)	9.8316(6)	7.2834(4)	4.1	2.01(1)	1.119
291	41:34:29	45	3.75	800	3.1318(2)	9.8436(6)	7.2998(4)	4.4	1.04(1)	1.115
327	45:46:44	45	5.62	800	3.1309(2)	9.7671(8)	7.2864(5)	14.6	−2.38(1)	1.145
339	47:26:34	45	3.82	800	3.1314(2)	9.8387(8)	7.3014(4)	5.0	1.23(1)	1.121
363	50:18:39	45	6.09	800	3.1311(2)	9.7394(8)	7.2888(6)	17.6	−2.41(2)	1.182
379	52:10:43	45	3.65	800	3.1327(2)	9.8431(7)	7.3019(5)	5.7	1.74(1)	1.113
381	52:29:51	45	3.92	1000	3.1361(2)	9.8559(7)	7.3161(5)	5.7	0.85(1)	1.114
422	57:17:00	45	5.30	1000	3.1374(2)	9.7914(7)	7.3064(5)	15.8	−1.26(1)	1.194
435	58:48:03	45	3.36	1000	3.1390(2)	9.8708(7)	7.3212(4)	5.0	1.14(1)	1.180
436	58:58:31	45	3.43	1000	3.1391(2)	9.8682(6)	7.3197(4)	5.0	0.97(1)	1.187
473	63:17:37	45	5.51	1000	3.1363(2)	9.7871(7)	7.3038(5)	15.4	−1.58(1)	1.205
493	65:40:39	45	3.25	1000	3.1403(2)	9.8714(7)	7.3220(5)	4.5	0.98(1)	1.176
494	65:58:24	45	3.57	1300	3.1475(2)	9.8924(5)	7.3422(4)	4.5	−0.03(1)	1.176
541	71:28:24	45	4.45	1300	3.1443(2)	9.8631(5)	7.3349(5)	14.7	−0.10(1)	1.238
560	73:43:26	45	3.61	1300	3.1477(2)	9.8889(7)	7.3427(5)	5.1	−0.05(1)	1.203
581	76:16:21	45	5.53	1300	3.1409(2)	9.8252(9)	7.3269(6)	20.8	−0.30(1)	1.305

F_2 is the texture index and is a measure of the texture sharpness.
[a] Image taken before start of experiment. Unit cell parameters fixed for refinement.

Diffraction images show that the starting material was initially randomly oriented and exhibited no significant lattice strains as would be expected (Fig. 4a). During quasi-hydrostatic pressure increase to 25 tons, at the start of deformation, a weak texture is induced in the sample (F_2=1.066). An IPF taken at 25 tons (1.95 GPa) prior to axial shortening shows a weak maximum toward the 010 direction and a small shoulder toward 011 (Fig. 5 #26). Upon commencement of axial shortening (#59), texture strength increases (F_2=1.132). The maximum near 010 becomes more pronounced and a minimum develops around 100. During lengthening back to 0% natural strain (#64), texture strength decreases but the distribution does not become completely random. The concentrated 010 texture observed during shortening weakens and becomes more diffuse (F_2=1.118). However, the 010 component never completely disappears. The minimum near 100 remains depleted and exhibits little change between shortening and lengthening textures. This pattern of textures for shortening and lengthening is consistent throughout the deformation experiment over the entire range of pressures and temperatures accessed (Figs. 5, 6).

At higher pressures, i.e. the 45 ton deformation cycles, the sample became much shorter on lengthening and could not be returned to 0% natural strain for fear of inducing brittle failure. As a consequence in the latter runs the sample was only brought to ~4% natural strain on extension. During shortening the sample was deformed to ≥15% natural strain so that texture changes from lengthening to shortening could be more readily observed.

Fig. 7 shows values for t and F_2 from Table 1 plotted with respect to elapsed time. Upon macroscopic shortening t becomes large and negative, indicating an axially compressive stress state. Upon lengthening the sample returned toward a neutral stress

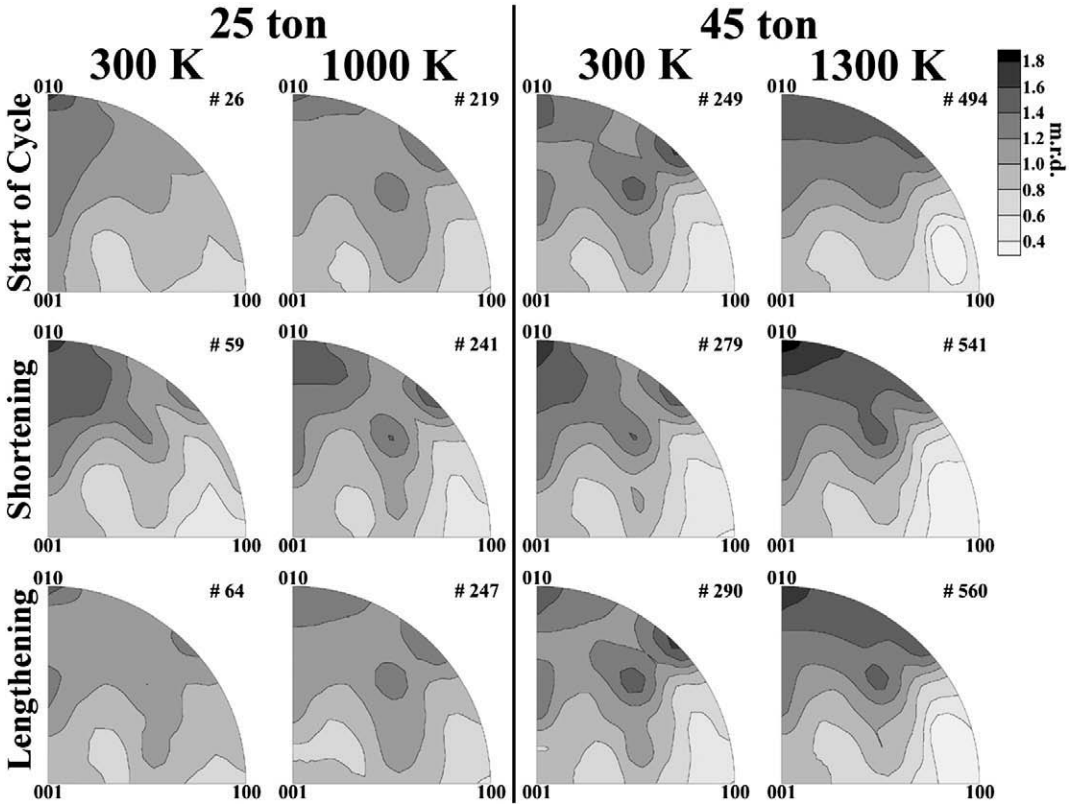

Fig. 5. Equal area projection IPFs for the 25 ton run at 300 K and 1000 K and the 45 ton run at 300 K and 1300 K. The top row shows the texture at the start of each cycle. The middle row shows the texture developed after shortening and the bottom row is after lengthening. Image numbers are indicated next to each pole figure and conditions are given in Table 1.

state (t=0 GPa), often overshooting and becoming slightly positive. F_2 increases upon shortening and decreases with lengthening. At high-temperatures, i.e. 25 ton, 1000 K and 45 ton, 1300 K runs, the absolute values of t decrease significantly compared to room temperature measurements and show much less variation with shortening and lengthening (Table 1 and Fig. 7). This is particularly pronounced in the 45 ton, 1300 K deformation cycle. During heating periods between deformation cycles, t becomes more neutral and relaxes toward 0 GPa, while F_2 remains relatively unchanged (Table 1 and Fig. 7).

5. Discussion

5.1. Texture and stress development

A 010 texture develops in all of the shortening cycles and weakens on lengthening. This pattern remains consistent even with repeated deformation cycles. Although the texture generated during lengthening shows minor variation, upon shortening the same texture is obtained. This pattern is similar for different pressures, temperatures and strain rates (Figs. 5, 6), indicating that these conditions have little effect on the texture type.

During the initial quasi-hydrostatic compression at room temperature to 25 tons, it is necessary for the user to monitor and adjust the differential rams to minimize differential stress resulting from different ram loading rates. This correction is performed manually and because of lag times, the sample experiences small variable shortening and lengthening episodes. Thus, even during this stage, the sample has already been subjected to small amounts of strain and exhibits associated texturing.

Toward the end of the experiment (45 ton 1000 K and 1300 K cycles), the values for F_2 show an overall increase

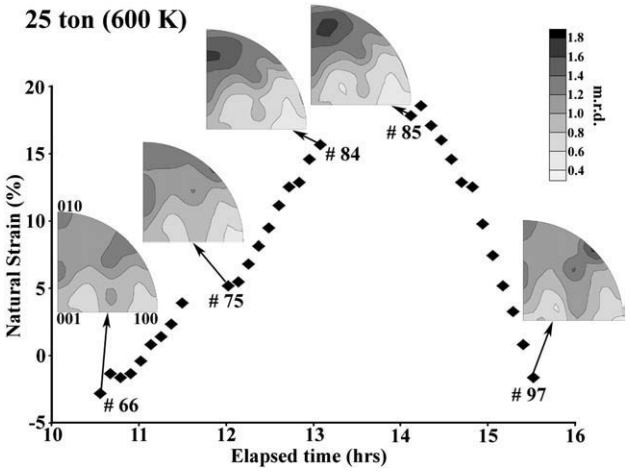

Fig. 6. Graph of natural strain vs. time for the 25 ton 600 K cycle. IPFs are shown for selected points along the deformation path. Arrows indicate points where textures are shown. Image numbers are given by points with textures shown and experimental conditions for these points are given in Table 1. IPFs are given in equal area projection.

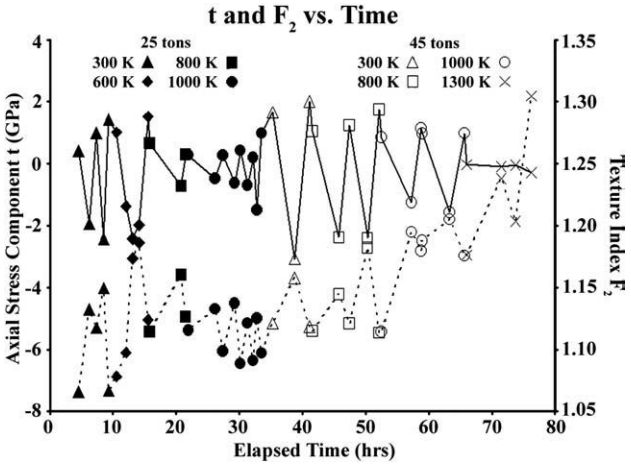

Fig. 7. The axial stress component (t) and texture index (F_2) plotted versus elapsed time. The solid line is t and the scale is given on the left. The dashed line is F_2 and scale is given on the right. Solid points are the 25 ton run and open points are the 45 ton run.

(Fig. 7, Table 1). This is partially due to the larger strain introduced near the end of the experiment, and is also consistent with the longer strain history. This trend, coupled with the overall decrease in the axial stress component at these conditions, indicates a softening of the yield strength. At the same time more deformation is accommodated by plastic processes such as slip, yielding stronger textures. This softening trend is also observed in the 25 ton cycles as well as the 45 ton cycles, where at higher temperatures, values for t are significantly reduced compared to lower temperature cycles. The effect on F_2 is most pronounced in the final deformation cycle with the higher confining pressure (45 tons) and highest temperature (1300 K) (Fig. 7, Table 1). Relaxation of stresses observed during heating periods in between deformation cycles are due to annealing of the sample, allowing elastic stresses to return to neutral (Fig. 7, Table 1).

5.2. Polycrystal plasticity modeling

By comparing textures generated with polycrystal plasticity models to experimental textures we can infer which slip systems are active under a given set of conditions. The development of textures depends on the deformation geometry and the relative activities of slip systems. For these simulations we used the Los Alamos viscoplastic self-consistent code (VPSC) (Lebensohn and Tomé, 1994). The VPSC model treats each grain as an inclusion in a homogeneous but anisotropic matrix that has the average properties of the polycrystal (Tomé and Canova, 2000). Starting with an initially random distribution of crystallite orientations and assuming deformation by intracrystalline slip, we apply an incremental deformation path. As deformation proceeds, crystals deform and rotate to generate preferred orientation. By applying different critical resolved shear stresses (CRSS) to slip systems, the model will favor one slip system over another. This will result in different textures for different slip system combinations. By determining which simulated texture most closely resembles the experimental texture, we can infer which slip systems are active under the experimental conditions.

For this model we started with a randomly oriented sample of 2000 grains and deformed in axial shortening to a total of 20% strain. We first investigated the effect of the slip plane on texture development. For this we ran seven models for slip on (100), (010), (001), {110}, {011}, {101}, and {111}, but allowing slip in many different directions (Fig. 8, Table 2). The only model

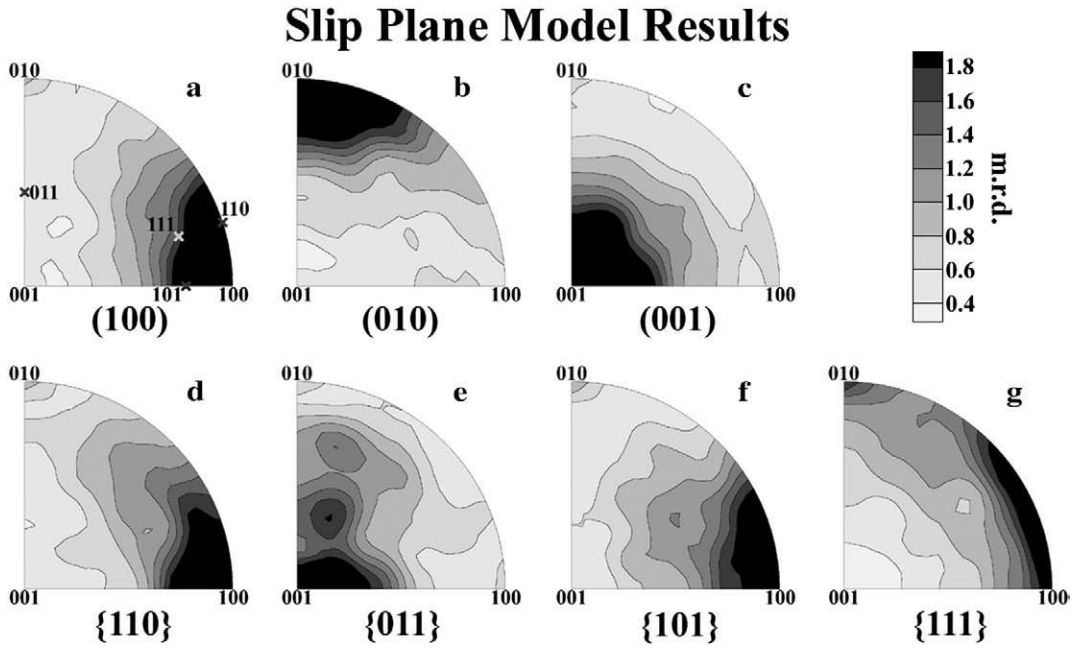

Fig. 8. Results from polycrystal plasticity simulations assuming activity of various slip systems for dominant slip on a) (100), b) (010), c) (001), d) {110}, e) {011}, f) {101}, and g) {111}. The only model that reproduces the maximum at (010) is model b) with dominant slip on the (010) plane.

Table 2
Summary of critical resolved shear stresses (CRSS) and slip system activities (ACT) in percent for the VPSC model results shown in Fig. 8

Figure	(100)[010], [001], ⟨011⟩		(010)[100], [001], ⟨101⟩		(001)[100], [010], ⟨110⟩		{110}⟨−110⟩, [001]		{011}⟨0−11⟩, [100]		{101}⟨−101⟩, [010]		{111}⟨101⟩	
	CRSS	ACT	CRSS	ACT	CRSS	ACT	CRSS	ACT	CRSS	ACT	CRSS	ACT	CRSS	ACT
a	1	97%	50	1%	50	1%	50	0%	50	1%	50	1%	100	0%
b	50	0%	1	97%	50	0%	50	1%	50	1%	50	1%	100	0%
c	50	0%	50	0%	1	97%	50	1%	50	1%	50	1%	100	0%
d	50	0%	50	0%	50	0%	1	100%	50	0%	50	0%	100	0%
e	50	0%	50	0%	50	0%	50	0%	1	100%	50	0%	100	0%
f	50	0%	50	0%	50	0%	50	0%	50	0%	1	100%	100	0%
g	50	1%	50	1%	50	0%	50	1%	50	1%	50	1%	1	95%

that reproduces that the maximum at (010), that is observed in experiment, is the model favoring dominant slip on the (010) and [100], [001], and ⟨101⟩ directions. Next we investigated specifically the effect of slip direction on the generated texture. We model slip on (010)[100], (010)[001], and (010)⟨101⟩. Slip systems activities and CRSS for these models are shown in Table 3. We find that preferential (010)[100] slip produces a distinct maximum around (010) and is the only model that produces a minimum near (100) as observed in experimental IPFs for $CaIrO_3$ pPv (Fig. 9). We also model lengthening favoring slip on (010)[100] (Fig. 9d) and compare to an experimental IPF obtained after lengthening back to ~5% natural strain. To perform this we used the texture obtained from modeling shortening with dominant (010)[100] slip (Fig. 9c) as our starting texture. The texture obtained from our lengthening model shows a diffuse maximum about (010) (Fig. 9d), that resembles the lengthening texture obtained experimentally. However it does not accurately reproduce the minimum near 100, and this may be due to grain shape or grain-to-grain interactions that are not included in the model. To assess the effect of sample history, we use a texture obtained experimentally at the end of a lengthening cycle as a starting texture in VPSC and model shortening with various slip systems. We do not observe a significant difference between these results and those that started with an initially random orientation. This indicates that in this case textures obtained with shortening are robust and that the sample history has little effect on the final texture generated during shortening. Overall dominant (010)[100] slip provides a good match to experimental data from both shortening and lengthening cycles (Fig. 9a, d) and we conclude that this is the dominant slip system at all conditions of these experiments.

5.3. Slip systems in post-perovskite

This result is consistent with TEM results by Miyajima et al. (2006), where dislocations with Burgers vector **b**=[100] and **b**=[u0w] were observed. Based on these observations the (010) plane was suggested as the slip plane. This slip plane is also consistent with room temperature DAC experiments on $CaIrO_3$ pPv (Niwa et al., 2007). The (010)[100] slip system has also been inferred based on EBSD orientation analysis of recovered samples (Yamazaki et al., 2006; Walte et al., 2007) and our *in-situ* results confirm this. Based on structural considerations, the (010) slip plane has also been suggested for $MgSiO_3$ pPv (Murakami et al., 2004; Oganov and Ono, 2004; and Iitaka et al., 2004). First-principles calculations of dislocation cores predict slip on (010)[001] for $MgSiO_3$ pPv (Carrez et al., 2007). This slip plane is the same as we suggest for $CaIrO_3$, however, the Burgers vector of [001] results in a very different texture than we obtain experimentally. Slip on (010)[001] produces two maxima, one offset from (010) and one at (100) with a distinct minimum around (100) (Fig. 9f), and this bears little resemblance to experimental IPFs (Fig. 5, 6).

Our results for $CaIrO_3$ pPv are in contrast with textures measurements on $MgGeO_3$ pPv (Merkel et al., 2006) and $MgSiO_3$ pPv (Merkel et al., 2007) in the DAC, where a maximum near (100) and a distinct minimum of (010) was observed (Fig. 10). This was interpreted as evidence for (100) and {110} slip, in agreement with first-principles calculations (Oganov et al., 2005). These calculations identified a family of polytypes that are intermediate to Pv and pPv structures with {110} as the dominant slip plane. The difference in textures between $CaIrO_3$ pPv and DAC measurements on $MgGeO_3$ pPv (Merkel et al., 2006) and $MgSiO_3$ pPv (Merkel et al., 2007) is

Table 3
Summary of CRSS and ACT in percent for VPSC model results shown in Fig. 9

Figure	(010)[100]		(010)⟨101⟩		(010)[001]		{110}⟨−110⟩		(100)[010]		(100)[001]		(001)[010]		(001)[100]		{011}[100]		{111}⟨101⟩	
	CRSS	ACT	CRSS	ACT	CRSS	ACT	CRSS	ACT	CRSS	ACT	CRSS	ACT	CRSS	ACT	CRSS	ACT	CRSS	ACT	CRSS	ACT
c	1	45%	50	10%	50	7%	50	11%	50	0%	50	6%	50	7%	50	6%	50	3%	100	6%
d[a]	1	45%	50	10%	50	6%	50	11%	50	0%	50	6%	50	6%	50	6%	50	3%	100	7%
e	50	0%	1	97%	50	0%	50	1%	50	0%	50	1%	50	0%	50	1%	50	0%	100	0%
f	50	6%	50	1%	1	45%	50	21%	50	6%	50	5%	50	0%	50	5%	50	6%	100	5%

Model d) is for lengthening back to 5% natural strain starting from the texture of c) all others are for shortening.
[a] Lengthening back to 5% strain starting with texture from model (c).

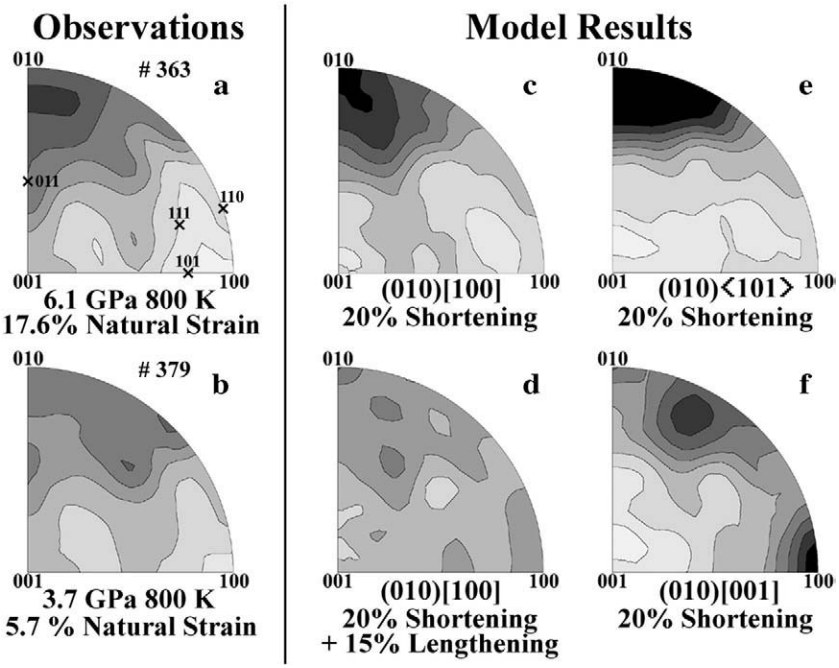

Fig. 9. Comparison of experimental IPFs a) after shortening and b) after lengthening, and model results for c) 20% shortening with dominant (010)[100] slip followed by d) 15% lengthening (back to 5% strain) with dominant (010)[100] slip, e) 20% shortening with dominant (010)〈101〉 slip and f) 20% shortening with dominant (010)[001] slip. The only model that reproduces both the maximum at (010) and the minimum at (100) is c), dominant slip on (010)[100]. Modeling lengthening using the starting texture of c) and (010)[100] slip yields d) which is similar to observed lengthening textures b).

unlikely due to activation of high-temperature slip systems, as $CaIrO_3$ pPv exhibits the same textures at room temperature as it does at high-temperature. Thus the difference must be due to some other cause, perhaps a different type of bonding.

Recent experiments on Mn_2O_3 pPv documented both of these texture types (Santillán et al., 2006). In this experiment polycrystalline Mn_2O_3 in an Ar pressure medium was compressed in the DAC and annealed to remove differential stresses. Prior to annealing it was observed that the (010) lattice planes were oriented perpendicular to compression. After annealing it was noted that lattice preferred orientation changed, with (100) and {110} planes at high angles to compression. It was proposed that the (010) texture is due to texture development under high differential stress, but could possibly be a transformation texture if displacement occurs along (010) during the phase transformation. The second texture of (100) and {110} may be due to annealing or a lower differential stress (Santillán et al., 2006). It should be noted that this experiment was performed in axial DAC geometry which is not ideal for the measurement of textures.

Here we rule out that the (010) texture in $CaIrO_3$ is the result of a phase transformation. The starting material is a polycrystalline, texture free, sintered sample of a single phase $CaIrO_3$ pPv. As all deformation cycles were performed within the stability field of the pPv phase and no phase transformation was observed with *in-situ* radial diffraction, the textures generated in this experiment are unequivocally deformation in origin. The second texture observed by Santillán et al. (2006) is similar to that observed in $MgGeO_3$ (Merkel et al., 2006) and $MgSiO_3$ pPv (Merkel et al., 2007) deformed in the DAC. It is possible that these textures are the result of annealing or deformation under lower differential stress. Annealing can cause significant changes in texture due to recrystallization and grain growth as observed *in-situ* in $(Mg_{0.75}Fe_{0.25})O$ (Kunz et al., 2007).

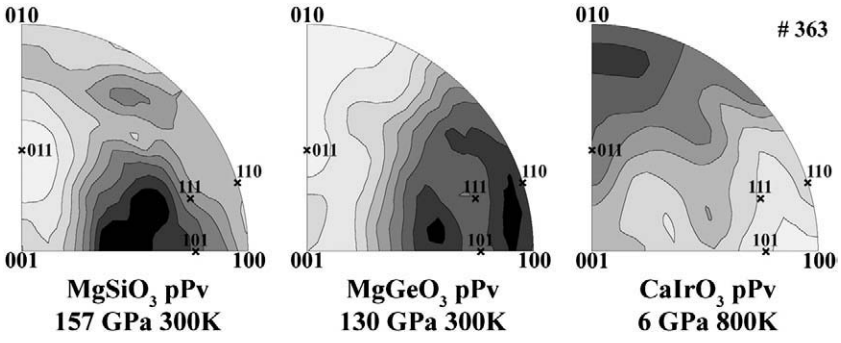

Fig. 10. A comparison of IPFs for various compression experiments on $MgGeO_3$ pPv (Merkel et al., 2006), $MgSiO_3$ pPv (Merkel et al., 2007), and $CaIrO_3$ pPv. $MgGeO_3$ pPv and $MgSiO_3$ pPv are best explained by dominant slip on the (100) and {110} planes while $CaIrO_3$ is best explained by slip on (010)[100].

Recrystallization may tend to annihilate plastically hard orientations in favor of softer orientations (Wenk et al., 1998). This results in a tendency for texture minima to become even more depleted while maxima become stronger, and would not explain the texture observed in Mn_2O_3 after annealing. Recrystallization is however a complex and poorly understood process (Gottstein, 2002). Under the conditions of the $CaIrO_3$ experiments no significant recrystallization occurred with no evidence for grain growth or change in grain shape at higher temperature.

Another explanation is that the interatomic potential between the layers in the pPv structure and the interlayer cations is different for $CaIrO_3$ and $MgSiO_3$ pPv. $CaIrO_3$ may behave as a sheet structure and slip along these layers. $MgSiO_3$ on the other hand has stronger coupling across the layers and slip does not occur along the layered structure. Similar differences in slip systems are well known for other structures such as calcite with dominant rhombohedral slip (Turner et al., 1954a) and dolomite with dominant basal slip (Turner et al., 1954b). $CaIrO_3$ pPv has very different structural parameters than $MgSiO_3$ pPv, such as bond length and angle as well as octahedral distortion. $MgGeO_3$ (and $NaMgF_3$) is much more similar to $MgSiO_3$ and may indicate that $MgGeO_3$ is a better analog for $MgSiO_3$ pPv (Kubo et al., submitted for publication). This conclusion is supported by this work and previous work in the DAC (Merkel et al., 2006, 2007), and may indicate that structural topology alone does not determine deformation behavior of pPv structured compounds and other parameters such as composition and bonding likely play a significant role. However were (010)[100] to be the dominant slip system in $MgSiO_3$ pPv at lower mantle conditions, this would have a considerable effect on seismic anisotropy and would yield a different pattern than predicted based on DAC results for $MgGeO_3$ (Merkel et al., 2006) and $MgSiO_3$ pPv (Merkel et al., 2007).

6. Conclusions

We plastically deform $CaIrO_3$ pPv in the D-DIA multi-anvil press at a range of pressures and temperatures up to 6 GPa and 1300 K. At all conditions, axial shortening induces a texture characterized by a maximum at (010) and a minimum near (100) in IPFs of the compression direction. This texture is compatible with dominant slip on the (010)[100]. This is in contrast with $MgGeO_3$ pPv (Merkel et al., 2006) and $MgSiO_3$ pPv (Merkel et al., 2007) which both show textures consistent with slip on (100) and {110} planes. As we see no change in texture in $CaIrO_3$ pPv with increased temperature, we conclude that this difference is not due to activation of high-temperature slip systems. The most likely explanation is that the two systems exhibit a different deformation behavior and $CaIrO_3$ may not be a good analog for the plastic behavior of pPv in the deep earth.

Acknowledgements

This work was performed at GeoSoilEnviroCARS (Sector 13), Advanced Photon Source (APS), Argonne National Laboratory. GeoSoilEnviroCARS is supported by the National Science Foundation — Earth Sciences (EAR-0622171) and Department of Energy — Geosciences (DE-FG02-94ER14466). Use of the Advanced Photon Source was supported by the U. S. Department of Energy, Office of Science, Office of Basic Energy Sciences, under Contract No. DE-AC02-06CH11357. We acknowledge support from CDAC (TD and HRW) and NSF (EAR-0337006). We are most appreciative for constructive comments by reviewers that helped to improve the manuscript.

References

Bunge, H.J., 1982. Texture Analysis in Materials Science — Mathematical Methods. Butterworths, London.

Carrez, P., Ferre, D., Cordier, P., 2007. Implications for plastic flow in the deep mantle from modelling dislocations in $MgSiO_3$ minerals. Nature 446, 68–70.

Fujibuchi, M., Tsuchiya, T., Tsuchiya, J., 2006. Elasticity of Cmcm $CaIrO_3$ Eos Trans. AGU 87 (52) Fall Meet. Suppl., Abstract MR11B-0126.

Gottstein, G., 2002. Evolution of recrystallization textures — classical approaches and recent advances. Mat. Sci. Forum 408–412, 1–24.

Guignot, N., Andrault, D., Morard, G., Bolfan-Casanova, N., Mezouar, M., 2007. Thermoelastic properties of post-perovskite phase $MgSiO_3$ determined experimentally at core–mantle boundary P–T conditions. Earth Planet. Sci. Lett. 256, 162–168.

Hammersley, A.P., 1997. ESRF Internal Report, ESRF97HA02T. FIT2D: An Introduction and Overview.

Iitaka, T., Hirose, K., Kawamura, K., Murakami, M., 2004. The elasticity of the $MgSiO_3$ post-perovskite phase in the Earth's lowermost mantle. Nature 430, 442–445.

Ischia, G., Wenk, H.R., Lutterotti, L., Berberich, F., 2005. Quantitative Rietveld texture analysis from single synchrotron diffraction images. J. Appl. Crystallogr. 8, 377–380.

Kubo, A., Kiefer, B., Shim, S.H., Shen, G., Prakapenka, V.B., Duffy, T.S., Rietveld structure refinement of $MgGeO_3$ post-perovskite phase to 1 Mbar, Am Mineralogist (submitted for publication).

Kunz, M., Caldwell, W.A., Miyagi, L., Wenk, H.R., 2007. *In situ* laser heating and radial synchrotron diffraction in a diamond anvil cell. Rev. Sci. Instrum. 78, 063907.

Lay, T., Williams, Q., Garnero, E.J., 1998. The core–mantle boundary layer and deep Earth dynamics. Nature 398, 461–468.

Lebensohn, R.A., Tomé, C.N., 1994. A self-consistent visco-plastic model: prediction of rolling textures of anisotropic polycrystals. Mater. Sci. Eng. A175, 71–82.

Lutterotti, L., Matthies, S., Wenk, H.R., 1999. MAUD: a friendly Java program for materials analysis using diffraction. Int. U. Crystallogr. Comm. Powder Diffr. Newslett. 21, 14–15.

Martin, C.D., Chapman, K.W., Chupas, P.J., Prakapenka, V., Lee, P.L., Shastri, S.D., Parise, J.B., 2007. Compression, thermal expansion, structure, and instability of $CaIrO_3$, the structure model of $MgSiO_3$ post-perovskite. Am. Mineral. 92, 1048–1053.

Matthies, S., Vinel, G.W., 1982. On the reproduction of the orientation distribution function of textured samples from reduced pole figures using the concept of conditional ghost correction. Phys. Status Solidi B, 112, K111–K114.

Matthies, S., Priesmeyer, H.G., Daymond, M.R., 2001. On the diffractive determination of single-crystal elastic constants using polycrystalline samples. J. Appl. Crystallogr. 34, 585–601.

Merkel, S., Kubo, A., Miyagi, L., Speziale, S., Duffy, T.S., Mao, H.K., Wenk, H.R., 2006. Plastic deformation of $MgGeO_3$ post-perovskite at lower mantle pressures. Science 311, 644–646.

Merkel, S., McNamara, A.K., Kubo, A., Speziale, S., Miyagi, L., Meng, Y., Duffy, T.S., Wenk, H.R., 2007. Deformation of $(Mg,Fe)SiO_3$ post-perovskite and D″ Anisotropy. Science 316, 1729–1732.

Miyagi, L., Merkel, S., Yagi, T., Sata, N., Ohishi, Y., Wenk, H.R., 2006. Quantitative Rietveld texture analysis of $CaSiO_3$ perovskite deformed in a diamond anvil cell. J. Phys., Condens. Matter 18, S995–S1005. doi:10.1088/0953-8984/18/27/S07.

Miyajima, N., Ohgushi, K., Ichihara, M., Yagi, T., 2006. Crystal morphology and dislocation microstructures of $CaIrO_3$: a TEM study of an analogue of the$MgSiO_3$ post-perovskite phase. Geophys. Res. Lett. 33, L12302. doi:10.1029/2005GL025001.

Murakami, M., Hirose, K., Kawamura, K., Sata, N., Ohishi, Y., 2004. Postperovskite phase transition in $MgSiO_3$. Science 304, 855–858.

Niwa, K., Yagi, T., Ohgushi, K., Merkel, S., Miyajima, N., Kikegawa, T., 2007. Lattice preferred orientation in $CaIrO_3$ perovskite and post-perovskite formed by plastic deformation under pressure. Phys. Chem. Miner. 34, 679–686.

Oganov, A.R., Ono, S., 2004. Theoretical and experimental evidence for a post-perovskite phase of $MgSiO_3$ in Earth's D″ layer. Nature 430, 445–448.

Oganov, A.R., Martonak, R., Laio, A., Raiteri, P., Parrinello, M., 2005. Anisotropy of Earth's D″ layer and stacking faults in the $MgSiO_3$ post-perovskite phase. Nature 438, 1142–1144.

Panning, M., Romanowicz, B., 2004. Inferences on flow at the base of Earth's mantle based on seismic anisotropy. Science 303, 351–353.

Rodi, V.F., Bable, D., 1965. Ternare Oxide Der Ubergangsmetalle. 4. Erdalkaliiridium(4)-Oxide — Kristallstruktur Von $CaIrO_3$. Z. Anorg. Allg. Chem. 336, 17.

Santillán, J., Shim, S.H., Shen, G., Prakapenka, V.B., 2006. High-pressure phase transition in Mn_2O_3: application for the crystal structure and preferred orientation of the $CaIrO_3$ type. Geophys. Res. Lett. 33, L15307. doi:10.1029/2006GL026423.

Shieh, S.R., Duffy, T.S., Kubo, A., Shen, G., Prakapenka, V.B., Sata, N., Hirose, K., Ohishi, Y., 2006. Equation of state of the post-perovskite phase synthesized from a natural $(Mg,Fe)SiO_3$ orthopyroxene. Proc. Natl. Acad. Sci. 103, 3039–3043.

Sidorin, I., Gurnis, M., Helmberger, D.V., 1999. Evidence for a ubiquitous seismic discontinuity at the base of the mantle. Science 286, 1326–1331.

Singh, A.K., 1993. The lattice strains in a specimen (cubic system) compressed nonhydrostatically in an opposed anvil device. J. Appl. Phys. 73, 4278–4286.

Singh, A.K., Balasingh, C., Mao, H.K., Hemley, R.J., Shu, J.F., 1998. Analysis of lattice strains measured under nonhydrostatic pressure. J. Appl. Phys. 83 (12), 7567–7575.

Stackhouse, S., Brodholt, J.P., Wookey, J., Kendall, J.M., Price, G.D., 2005. The effect of temperature on the seismic anisotropy of the perovskite and post-perovskite polymorphs of $MgSiO_3$. Earth Planet. Sci. Lett. 230, 1–10.

Tomé, C.N., Canova, G.R., 2000. Self-consistent modeling of heterogeneous plasticity. In: Kocks, U.F., Tomé, C.N., Wenk, H.-R. (Eds.), Texture and Anisotropy: Preferred Orientations in Polycrystals and their Effect on Materials Properties. Cambridge University Press, Cambridge, pp. 466–510.

Turner, F.J., Griggs, D.T., Heard, H.C., 1954a. Experimental deformation of calcite crystals. Bull. Geol. Soc. Am. 65, 883–934.

Turner, F.J., Griggs, D.T., Heard, H., Weiss, L.E., 1954b. Plastic deformation of dolomite rock at 380 ° C. Am. J. Sci. 252, 477–488.

Walte, N., Heidelbach, F., Miyajima, N., Frost, D., 2007. Texture development and TEM analysis of deformed $CaIrO_3$: implications for the D″ layer at the core–mantle boundary. Geophys. Res. Lett. 34, L08306. doi:10.1029/2007GL029407.

Wang, Y., Durham, W.B., Getting, I.C., Weidner, D.J., 2003. The deformation-DIA: a new apparatus for high temperature triaxial deformation to pressures up to 15 GPa. Rev. Sci. Instrum. 74, 3002–3011.

Wenk, H.R., Canova, G., Brechet, Y., Flandin, L., 1998. A deformation-based model for recrystallization of anisotropic materials. Acta Mater. 45 (8), 3283–3296.

Wenk, H.R., Ischia, G., Nishiyama, N., Wang, Y., Uchida, T., 2005. Texture development and deformation mechanisms in ringwoodite. Phys. Earth Planet. Inter. 152, 191–199.

Wenk, H.R., Lonardelli, I., Merkel, S., Miyagi, L., Pehl, J., Speziale, S., Tommaseo, C.E., 2006. Deformation textures produced in diamond anvil experiments, analysed in radial diffraction geometry. J. Phys., Condens. Matter 18, S933–S947. doi:10.1088/0953-8984/18/25/S02.

Wentzcovitch, R.M., Tsuchiya, T., Tsuchiya, J., 2006. $MgSiO_3$ post-perovskite at D″ conditions. Proc. Natl. Acad. Sci. 103, 543.

Wysession, M., Lay, T., Revenaugh, J., Williams, Q., Garnero, E.J., Jeanloz, R., Kellogg, L., 1998. The D″ discontinuity and its implications. In: Gurnis, M., Wysession, W.E., Knittle, E., Buffett, B.A. (Eds.), The Core–Mantle Boundary Region. AGU, Washington DC, pp. 273–298.

Yamazaki, D., Yoshino, T., Ohfuji, H., Ando, J., Yoneda, A., 2006. Origin of seismic anisotropy in the D″ layer inferred from shear deformation experiments on post-perovskite phase. Earth Planet. Sci. Lett. 252, 372–378.

Yoshino, T., Yamazaki, D., 2007. Grain growth kinetics of $CaIrO_3$ perovskite and post-perovskite, with implications for rheology of D″ layer. Earth Planet. Sci. Lett. 255, 485–493.